Journal of Materials Chemistry A

ROYAL SOCIETY OF CHEMISTRY

PAPER

View Article Online
View Journal | View Issue

Cite this: J. Mater. Chem. A, 2024, 12, 8796

Constructing oxygen vacancies by doping Mo into spinel Co_3O_4 to trigger a fast oxide path mechanism for acidic oxygen evolution reaction†

Lang Sun, Min Feng, Yang Peng, Xu Zhao, Yiqun Shao, Xin Yue * and Shaoming Huang *

Received 29th January 2024
Accepted 4th March 2024

DOI: 10.1039/d4ta00655k

rsc.li/materials-a

The development of non-precious metal electrocatalysts for acidic oxygen evolution reaction (OER) that are highly durable, cost-effective, and efficient is crucial to advancing the use of proton exchange membrane water electrolyzers (PEMWEs). Because of its reasonable activity and stability, spinel Co_3O_4 is regarded as a potential candidate for acidic OER. However, it is still far from industrial requirements owing to the sluggish adsorbate evolution mechanism (AEM) for the OER in acids. Herein, we report the enhancement of the activity and stability of acidic OER on Co_3O_4 by doping a small amount of Mo (~0.5 wt%). The oxygen vacancies are created by doping Mo to activate the lattice oxygen followed by etching away from the lattice, effectively promoting the fast oxide path mechanism (OPM) for the OER. Meanwhile, its stability is boosted by introducing Mo with variable valence states. As a result, as-fabricated Mo-doped oxygen vacancy enriched Co_3O_4 (V_O-$Mo_xCo_{3-x}O_4$) exhibits efficient activity with a current density of 100 mA cm^{-2} at an overpotential of 490 mV and Tafel slope of 102.5 mV dec^{-1} towards acidic OER. Meanwhile, V_O-$Mo_xCo_{3-x}O_4$ exhibits high stability and can maintain a current density of 10 mA cm^{-2} for 30 h.

Introduction

The production of hydrogen (H_2) through electrochemical water splitting is considered to offer a means of storing renewable electricity in the form of H_2 molecules.[1] The proton exchange membrane water electrolyzer (PEMWE) is recognized as a promising alternative to the alkaline water electrolyzer due to its superior gas purity and conversion efficiency, lower ohmic loss, higher current density, stable operational performance, and so on.[2] However, the oxygen evolution reaction (OER) in an acidic medium involves a four-electron–proton transfer process and the formation of O–O bonds, which necessitates a high overpotential to overcome the energy barrier, thereby resulting in sluggish kinetics.[2,3] The rapid decline in catalytic activity poses a more severe challenge for electrocatalysts, because they work in harsh environments, including at low pH values (~1), high potential windows, and saturated oxygen concentrations.[3,4] Precious metal-based electrocatalysts, such as IrO_2 and RuO_2, exhibit satisfactory activity for acidic OER. However, their high cost, limited resources, and poor stability greatly hinder the practical implementation.[5] Consequently, it is crucial to promote the widespread use of PEMWEs by developing non-precious metal electrocatalysts with high efficiency, stability and low cost.

By virtue of its relatively high activity and stability, spinel Co_3O_4 is considered to have potential to replace precious metal-based electrocatalysts for acidic OER.[6] However, owing to the slower adsorbate evolution mechanism (AEM) on the surface of Co_3O_4 for the OER, it is still far from realistic requirements. Three oxygen reaction intermediates of *OH, *O, and *OOH are generated and transformed during the AEM pathway (* denotes an active site). The binding energies of these intermediates adsorbed on the electrocatalysts are linearly correlated and therefore follow a scaling relationship.[7] This restriction makes a large theoretical overpotential of approximately 370 mV necessary to drive the OER *via* the AEM pathway.[8] Some electrocatalysts have reportedly shown increased activity surpassing the theoretical limit because they catalyze the OER through a kinetically favorable lattice-oxygen-mediated mechanism (LOM). Lattice oxygen and O-radicals combine to form oxygen gas, preventing the production of *OOH.[9] Nevertheless, the formation of oxygen vacancies during the LOM process leads to the etching away of metal species from surfaces, which causes the electrocatalysts to degrade quickly.[10] The recently reported oxide path mechanism (OPM), which allows direct oxygen radical self-coupling to be the oxygen bridge (O–O) without generating oxygen vacancies and additional intermediates like *OOH, is deemed to be the fastest and most stable pathway for

Guangzhou Key Laboratory of Low-Dimensional Materials and Energy Storage Devices, Collaborative Innovation Center of Advanced Energy Materials, School of Materials and Energy, Guangdong University of Technology, Guangzhou, 510006, P. R. China. E-mail: xinyue@gdut.edu.cn; smhuang@gdut.edu.cn

† Electronic supplementary information (ESI) available. See DOI: https://doi.org/10.1039/d4ta00655k

the OER in an acidic environment.[11] The design of non-precious metal electrocatalysts for the OER in an acidic solution to undergo the OPM pathway, thus, calls for a feasible strategy.

To the best of our knowledge, the OPM pathway for the OER in acid has been found only on limited electrocatalysts, primarily Ru-based heterogeneous catalysts, such as Ru-MOF-400 and 12Ru/MnO_2.[11–13] Building oxygen vacancies has been reportedly presented to effectively enhance the activity of the OER in alkaline media by triggering the OPM pathway on Co_3O_4.[14,15] However, when applying this strategy in an acidic medium, Co_3O_4 would be rapidly degraded in acidic electrolyte owing to the oxygen vacancy enriched surface, which eventually causes the activity to drop.[16] Fortunately, it has been proposed that modulating the d-band structure of Co by doping or substituting metal-cations such as Mn, Ti, Mo, and so on with variable valence states into Co_3O_4 can efficiently improve the stability of acidic OER.[17–19] In recent years, introducing cations with variable valence states, for example, Mn, into the lattice of spinel Co_3O_4 has been proven to improve the stability of acidic OER on the as-synthesized electrocatalysts.[17,18] This is because the introduced cations would be oxidized to higher valence states during the OER process. This oxidative conversion would transfer the electrons to the closest Co sites, which reduces the valence states of Co^{3+} species to the more stable Co^{2+} species.[17] Meanwhile, the O 2p band center is typically upshifted by introducing Mo into metal oxide, which weakens the metal–oxygen bonds and ultimately builds oxygen vacancies inside metal oxide.[20]

Therefore, in this report, an approach of doping a small amount of Mo (~0.5 wt%) into Co_3O_4 is reported to enhance the activity and stability of the OER in acidic media since it can activate the lattice oxygen to be etched away from the lattice for creating oxygen vacancies. The generated oxygen vacancies can effectively promote the fast OPM pathway, and simultaneously the introduction of Mo with variable valence states will improve the stability. We successfully prepare a very small amount of Mo-doped oxygen vacancy enriched Co_3O_4 (V_O-$Mo_xCo_{3-x}O_4$) through hydrothermal treatment followed by annealing under an air atmosphere. As a result, Co_3O_4 requires an overpotential of 490 mV to attain a current density of 10 mA cm^{-2}. Owing to the fast OPM pathway triggered by creating oxygen vacancies in its lattice, as-fabricated V_O-$Mo_xCo_{3-x}O_4$ exhibits an enhanced activity, which reaches 10 and 100 mA cm^{-2} at overpotentials of 420 and 490 mV, respectively, being superior to Ir/C. Meanwhile, V_O-$Mo_xCo_{3-x}O_4$ possesses the fastest kinetics (with a Tafel slope of only 102.5 mV dec^{-1}) towards the OER in acid when compared with those of pure Co_3O_4 and Ir/C electrocatalysts. V_O-$Mo_xCo_{3-x}O_4$ exhibits high stability towards acidic OER and can maintain a current density of 10 mA cm^{-2} for 30 h. The mechanism for enhancing the OPM on V_O-$Mo_xCo_{3-x}O_4$ has been studied by detailed characterization together with theoretical calculations.

Results and discussion

The synthetic route for V_O-$Mo_xCo_{3-x}O_4$ is schematically illustrated in Fig. 1a, involving hydrothermal treatment followed by the annealing process under an air atmosphere. Cobalt nitrate hexahydrate ($Co(NO_3)_2 \cdot 6H_2O$) and ammonium molybdate tetrahydrate ($(NH_4)_6Mo_7O_{24} \cdot 4H_2O$) were used as the precursors of Co and Mo elements, respectively. Mo doped $Co(OH)_2$ ($Co_{1-x}Mo_x(OH)_2$) was generated after hydrothermal treatment as the intermediate (Fig. S1 in the ESI†). Lattice oxygen was then activated to be etched away from the as-prepared $Mo_xCo_{3-x}O_4$ when it was annealed under an air atmosphere. Inductively coupled plasma atomic emission spectroscopy (ICP-AES) was used to determine the atomic ratio of Mo to Co in V_O-$Mo_xCo_{3-x}O_4$, which is about 1 : 230. Thus, the amount of Mo in V_O-$Mo_xCo_{3-x}O_4$ can be obtained to be ~0.5 wt%. For comparison, pure Co_3O_4 was also prepared through a similar method (for details see the Experimental section, ESI†). X-ray diffraction (XRD) was used to investigate the crystal structures of V_O-$Mo_xCo_{3-x}O_4$ and Co_3O_4, as shown in Fig. 1b. In the XRD patterns of V_O-$Mo_xCo_{3-x}O_4$ and Co_3O_4, the diffraction peaks at 19.0°, 31.3°, 36.8°, 38.5°, 44.8°, 55.7°, 59.4°, and 65.2° correspond to the (111), (220), (311), (222), (400), (422), (511) and (440) facets of cubic spinel Co_3O_4 (PDF# 42-1467).[17]

The lattice dynamics of V_O-$Mo_xCo_{3-x}O_4$ and Co_3O_4 were confirmed by Raman and Fourier transform infrared (FT-IR) spectroscopy (Fig. 1c, S2 and S3, ESI†). A_{1g}, E_g, and three F_{2g} modes are the five typical Raman active modes of cubic spinel oxides with an $Fd\bar{3}m$ space group,[21] as shown in Fig. 1c. The A_{1g} mode is related to the Co^{3+}–O stretching in the octahedral CoO_6 unit, and the F'_{2g} mode corresponds to the Co^{2+}–O stretching in the tetrahedral CoO_4 geometry.[22,23] The A_{1g} mode in the Raman spectrum of V_O-$Mo_xCo_{3-x}O_4$ at 655.4 cm^{-1}, has been found to red-shift by 7.9 cm^{-1} compared to that of Co_3O_4 (Fig. S2, ESI†). This is ascribed to the lattice disorder increased by oxygen vacancies.[24] The intensity ratio of the A_{1g} to F'_{2g} band ($I_{A_{1g}}/I_{F'_{2g}}$) shows the occupied degree of octahedral sites.[25] $I_{A_{1g}}/I_{F'_{2g}}$ of V_O-$Mo_xCo_{3-x}O_4$ is 1.20, which is lower than that of Co_3O_4 (1.37). This is related to the presence of Co vacancies caused by the oxidation of the closest Mo cations.[26,27] The FT-IR results can also be used to identify similar situations involving the variation in octahedral sites (Fig. S3, ESI†). Electron paramagnetic resonance (EPR) spectroscopy was employed to examine the structure of defects in V_O-$Mo_xCo_{3-x}O_4$ since it is sensitive to unpaired electrons, as illustrated in Fig. 1d. In the EPR spectrum of Co_3O_4, there is no discernible signal, indicating a pure crystal without defects. The EPR spectrum of V_O-$Mo_xCo_{3-x}O_4$ shows a sharp increase in the intensity of the *g*-factor at 2.003, suggesting the successful construction of oxygen vacancies by doping Mo into Co_3O_4.[28]

Scanning electron microscopy (SEM) and transmission electron microscopy (TEM) techniques were used to analyze the morphologies of V_O-$Mo_xCo_{3-x}O_4$ and Co_3O_4 (Fig. 1e–i and S4, ESI†). V_O-$Mo_xCo_{3-x}O_4$ consists of nanoparticles with sizes ranging from 50 to 500 nm (Fig. 1e). A similar morphology of Co_3O_4 can be observed in the SEM image as well (Fig. S4a†). A typical TEM image of V_O-$Mo_xCo_{3-x}O_4$ with a particle size of 200 nm is depicted in Fig. 1f. As observed in the high-resolution TEM (HR-TEM) image of V_O-$Mo_xCo_{3-x}O_4$ in Fig. 1g, the interplanar spacings of 0.24 and 0.46 nm can be assigned to the (311) and (111) facets of V_O-$Mo_xCo_{3-x}O_4$, respectively. Additionally,

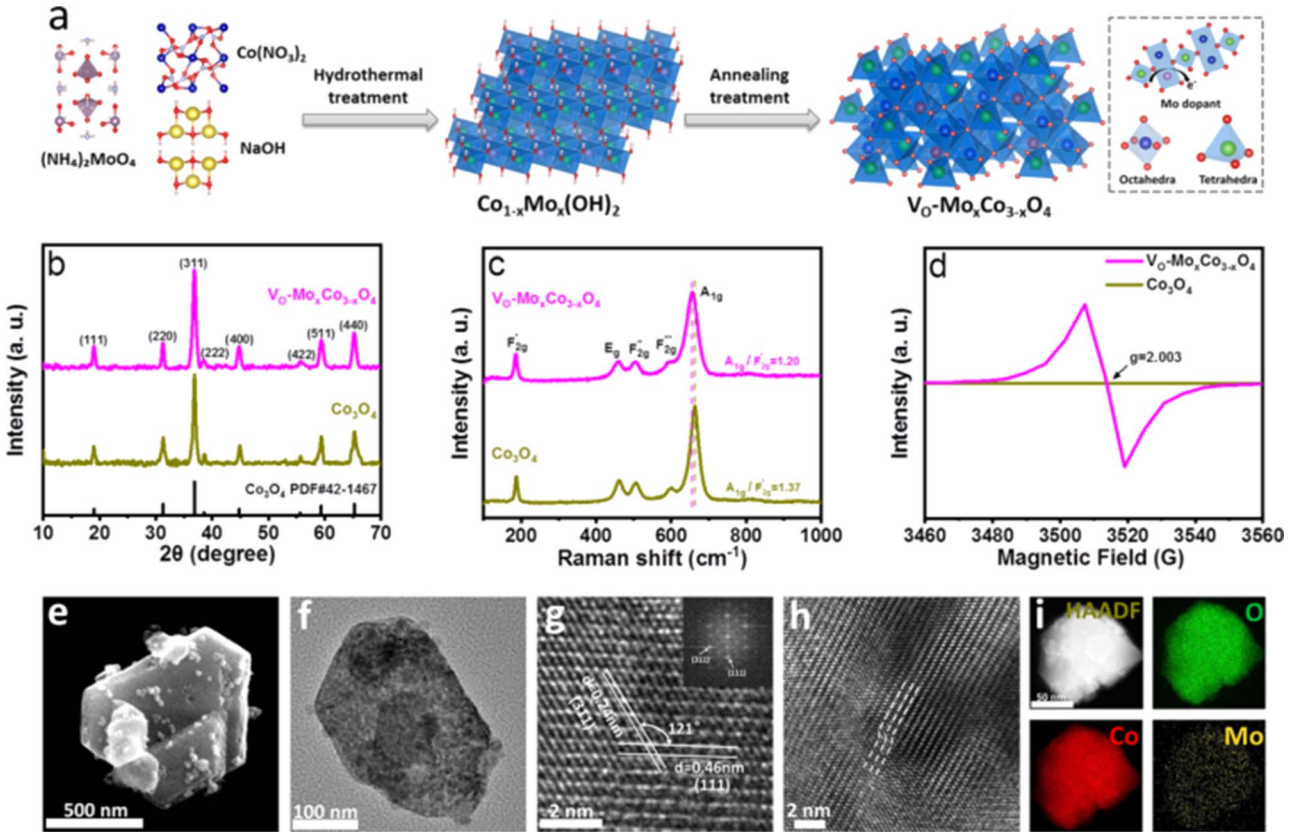

Fig. 1 (a) Scheme of the synthetic process for V_O-$Mo_xCo_{3-x}O_4$. (b) XRD patterns of V_O-$Mo_xCo_{3-x}O_4$ and Co_3O_4. (c) Raman spectra of V_O-$Mo_xCo_{3-x}O_4$ and Co_3O_4. (d) EPR spectra of V_O-$Mo_xCo_{3-x}O_4$ and Co_3O_4. (e) SEM image of V_O-$Mo_xCo_{3-x}O_4$. (f–h) TEM images of V_O-$Mo_xCo_{3-x}O_4$. (i) HAADF-STEM and corresponding elemental mapping images of V_O-$Mo_xCo_{3-x}O_4$.

the HR-TEM image of Co_3O_4 shows the crystal indices of 0.24 and 0.28 nm, respectively, which is corresponding to the (311) and (220) planes of Co_3O_4 (Fig. S4c†). Moreover, lattice distortion can be observed in the TEM image of V_O-$Mo_xCo_{3-x}O_4$ presented in Fig. 1h, which originates from the lattice strain caused by doping Mo with a larger radius and creating oxygen vacancies.[29] The uniform distribution of Co, Mo, and O elements can be found across V_O-$Mo_xCo_{3-x}O_4$ according to the high angle annular dark field-scanning transmission electron microscope (HAADF-STEM) and corresponding elemental mapping images (Fig. 1i). Similar situations regarding the distribution of elements can be also observed for Co_3O_4 (Fig. S4d–f, ESI†).

X-ray photoelectron spectroscopy (XPS) was used to study the surface chemical state of V_O-$Mo_xCo_{3-x}O_4$ and Co_3O_4 (Fig. S5–S8, ESI†), which suggests lower valence states of Co along with a higher concentration of oxygen vacancies in V_O-$Mo_xCo_{3-x}O_4$. According to the results of XPS spectroscopy, the atomic ratio of Mo to Co in the near-surface of V_O-$Mo_xCo_{3-x}O_4$ is obtained to be 3 : 247 (Table S1, ESI†). Based on the result of ICP, the total atomic ratio of Mo to Co in V_O-$Mo_xCo_{3-x}O_4$ is 1 : 230. Therefore, Mo cations should mainly be distributed in the near-surface of V_O-$Mo_xCo_{3-x}O_4$. X-ray absorption fine structure spectroscopy (XAFS) was performed to investigate the electronic structure and coordination environment of V_O-$Mo_xCo_{3-x}O_4$ (Fig. 2). The X-ray absorption near edge structure (XANES) spectra of Co K edges for V_O-$Mo_xCo_{3-x}O_4$, Co_3O_4 and other compounds are displayed in Fig. 2a. As observed in the XANES spectra, CoO and Co_2O_3 display white line intensities at 7725.1 and 7730.3 eV, corresponding to Co^{2+} and Co^{3+}, respectively. The XANES spectrum of Co_3O_4 presents a white line intensity at 7729.2 eV, suggesting the coexistence of Co^{2+} and Co^{3+} in the lattice,[30] while V_O-$Mo_xCo_{3-x}O_4$ exhibits a white line intensity at 7729.0 eV, representing a decline of valence states of Co compared with that of Co_3O_4. Additionally, by examining the absorption energy location of the highest peak of the first derivative for the Co K-edge XANES spectra, the valence states of Co cations in various materials can be calculated[31] (Fig. 2b and S9, ESI†). The average valence state of Co in V_O-$Mo_xCo_{3-x}O_4$ is obtained to be $Co^{2.72+}$, which is slightly lower than that of Co_3O_4 ($Co^{2.76+}$) (Fig. 2b). This should be attributed to the creation of oxygen vacancies to lead to a lower coordination number with oxygen, and the doping of Mo cations with lower electronegativity.[32] In general, a lower valence state is in favour of enhancing the stability towards the OER because it will prevent the dissolution of Co into acidic solutions during the OER process.[33,34]

The Fourier transform (FT) Co K-edge extended X-ray absorption fine structure (EXAFS) spectra used to further analyze the coordination environments of V_O-$Mo_xCo_{3-x}O_4$ and Co_3O_4 are depicted in Fig. 2c. The peak at around 1.5 Å is

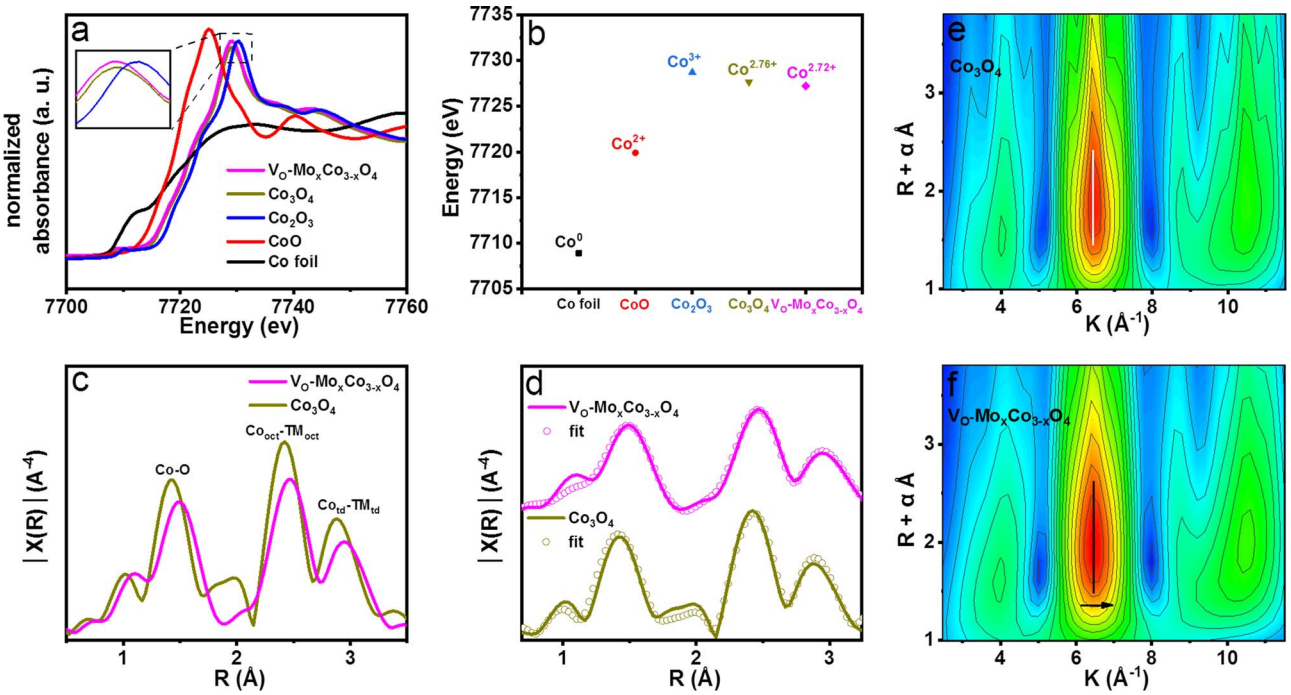

Fig. 2 (a) Normalized XANES spectra at the Co K-edge of V_O-$Mo_xCo_{3-x}O_4$, Co_3O_4 and comparisons. (b) Relationships between valence states and positions of the highest peak in the first derivative of XANES spectra at the Co K-edge of V_O-$Mo_xCo_{3-x}O_4$, Co_3O_4 and reference materials. (c) Resulting Fourier-transform (FT) k^3 weighted $\chi(k)$-function of Co K-edge EXAFS spectra for V_O-$Mo_xCo_{3-x}O_4$ and Co_3O_4. (d) Experimental data and fits of the Co K-edge EXAFS spectra for V_O-$Mo_xCo_{3-x}O_4$ and Co_3O_4. Wavelet transforms (WT) for the k^3 weighted EXAFS contour plots of (e) Co_3O_4 and (f) V_O-$Mo_xCo_{3-x}O_4$.

typically attributed to the TM–O bonds.[35] The peak at around 2.5 Å is assigned to the bonds between the nearest octahedral cations (TM_{oct}–TM_{oct}).[36] The peak at ~3.0 Å is a characteristic peak for tetrahedral cations (TM_{td}), representing the bonds between tetrahedral cations with the closest octahedral (TM_{oct}–TM_{td}) and tetrahedral (TM_{td}–TM_{td}) cations.[37] In addition, the experimental EXAFS spectra of V_O-$Mo_xCo_{3-x}O_4$ and Co_3O_4 were well-fitted to the cubic structure of Co_3O_4 ($Fd\bar{3}m$) (Fig. 2d and Table S2, ESI†). As a result, the amplitude of the Co–O characteristic peak in the EXAFS spectrum of V_O-$Mo_xCo_{3-x}O_4$ decreases when compared with that of Co_3O_4, suggesting the successful formation of oxygen vacancies in octahedral geometry.[38] Meanwhile, the bond length of Co–O in V_O-$Mo_xCo_{3-x}O_4$ is found to be larger than that of Co_3O_4, which is fitted to be a Co_{oct}–O bond with a coordination number (CN) of 5.375 and a bond length of 1.994 Å (Table S2, ESI†). While the Co_{oct}–O bond in Co_3O_4 is fitted to be a CN of 6.160 and a bond length of 1.953 Å. This may be related to the modulation of the electronic structure of Co cations by introducing oxygen vacancies and doping Mo with variable valence states into the lattice, which results in a decrease in the average valence states of Co, thereby regulating the Co–O bonds in TMO_6 units.[39] Furthermore, the amplitudes of the octahedral and tetrahedral characteristic peaks in the spectrum of V_O-$Mo_xCo_{3-x}O_4$ are observed to decrease, corresponding to the creation of Co_{oct} defects by inducing the oxidation of the nearest Mo cations.[40] The fitted bond length of Co_{oct}–Co_{oct} in V_O-$Mo_xCo_{3-x}O_4$ is 2.869 Å, which is slightly longer than that of Co_3O_4 (2.861 Å), resulting in a right-shift of the Co_{oct} characteristic peak in the EXAFS spectrum. Generally, it is considered to match well with the bond length of the O–O radical for enhancing the OPM pathway when the distance of the neighboring active sites is regulated to be 2.8–2.9 Å.[11–13] Co_{oct} is believed to be the real active species of spinel oxides for the OER because it is preferentially exposed on the surface.[38,39] Therefore, owing to the appropriate distance of Co_{oct}–Co_{oct}, V_O-$Mo_xCo_{3-x}O_4$ and Co_3O_4 have been deemed to have the conditions to achieve the OPM pathway for acidic OER.[13] The wavelet transform (WT) of the k^3-weighted EXAFS spectra at the V_O-$Mo_xCo_{3-x}O_4$ and Co_3O_4 Co K edges are shown in Fig. 2e and f. When compared to Co_3O_4, the Co_{oct}–Co_{oct} coordination characteristics of V_O-$Mo_xCo_{3-x}O_4$ exhibit a slight right-shift. This is connected to doping of the heavier element of Mo into V_O-$Mo_xCo_{3-x}O_4$.[41]

The effects on the performance of acidic OER by creating oxygen vacancies in Co_3O_4 were examined by obtaining the linear sweep voltammogram (LSV) curve of V_O-$Mo_xCo_{3-x}O_4$ in 0.1 M $HClO_4$ solution (Fig. 3a). Polarization curves of the OER were obtained on a Co_3O_4, Ir/C carbon paper electrode for comparison as well. All polarization curves were *iR*-corrected. It is worth noting that the synthetic condition for V_O-$Mo_xCo_{3-x}O_4$ was optimized (for details see Experimental section and Fig. S10, ESI†). As displayed in Fig. 3a, the carbon paper used as a working electrode only exhibits ignorable activity towards OER in acidic media. Ir/C has been proven to be oxidized to IrO_2/C during the catalytic process.[42] At an overpotential of 460 mV, the Ir/C electrocatalyst can reach a current density of 10 mA cm^{-2}.

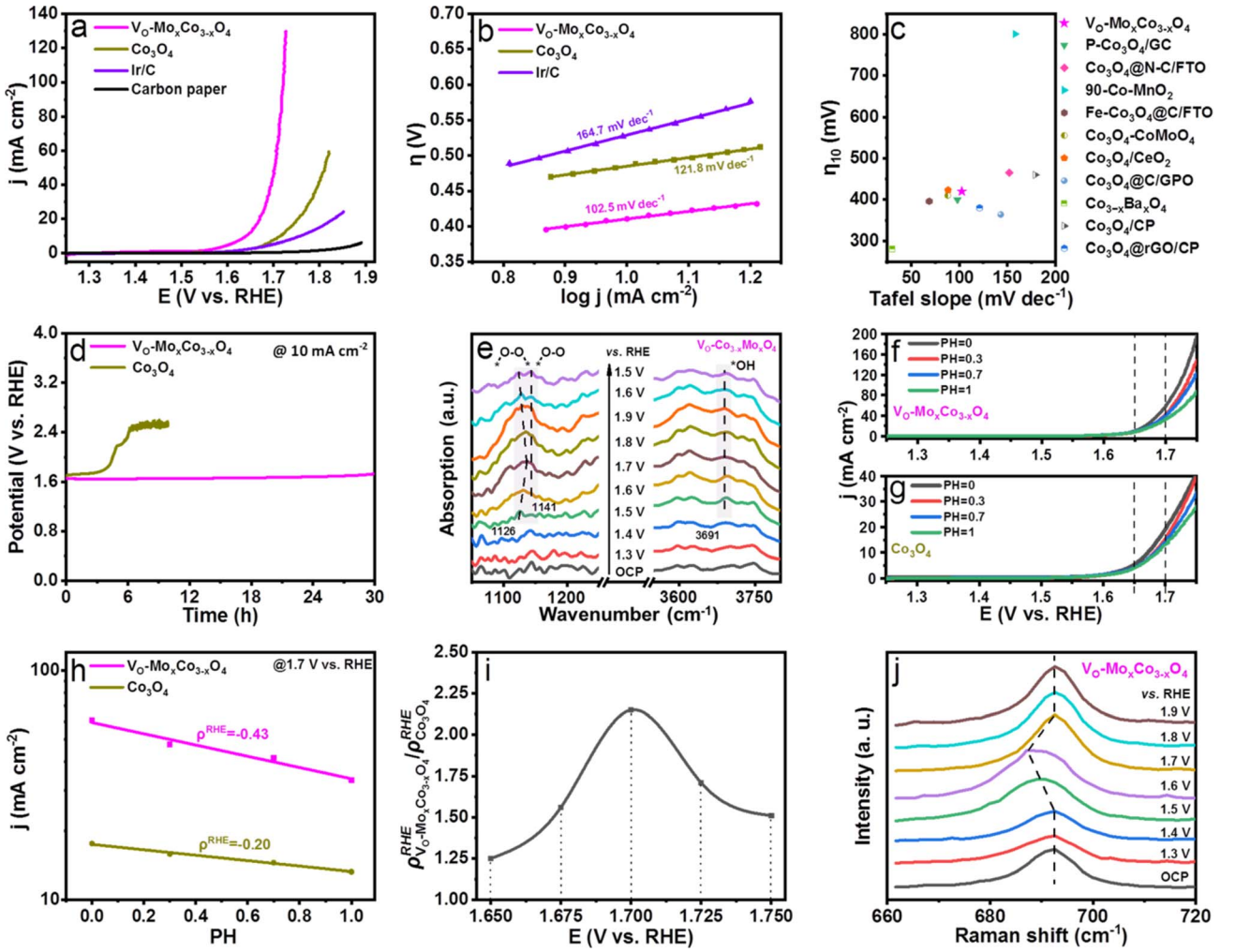

Fig. 3 (a) LSV curves of the OER on V_O-$Mo_xCo_{3-x}O_4$, Co_3O_4, Ir/C and carbon paper electrocatalysts in 0.1 M $HClO_4$ at 25 °C with scan rates of 5 mV s^{-1}. (b) Tafel plots of V_O-$Mo_xCo_{3-x}O_4$, Co_3O_4, Ir/C and carbon paper electrocatalysts. (c) Comparisons of Vo-$Mo_xCo_{3-x}O_4$ in terms of activity and kinetics with currently reported state-of-the-art non-precious metal electrocatalysts for acidic OER. (d) The chronopotentiometric curves of the OER on V_O-$Mo_xCo_{3-x}O_4$ and Co_3O_4 electrocatalysts at 10 mA cm^{-2} in 0.1 M $HClO_4$ (25 °C). (e) *In situ* FT-IR spectra recorded at various applied potentials (*vs.* RHE) in 0.1 M $HClO_4$ electrolyte on (a) V_O-$Mo_xCo_{3-x}O_4$. LSV curves of (f) V_O-$Mo_xCo_{3-x}O_4$ and (g) Co_3O_4 in acid electrolytes with different pH values. (h) OER specific activities of V_O-$Mo_xCo_{3-x}O_4$ and Co_3O_4 at 1.7 V *vs.* RHE against the pH values. (i) Relationship between the ratios of (ρ^{RHE} V_O-$Mo_xCo_{3-x}O_4$/ρ^{RHE} Co_3O_4) at different potentials. (j) *In situ* Raman spectra of V_O-$Mo_xCo_{3-x}O_4$ obtained on stepping the potential from 1.3 to 1.9 V *vs.* RHE in 0.1 M $HClO_4$ electrolyte.

When compared to Ir/C, Co_3O_4 shows inferior activity for OER, which can achieve a current density of 10 mA cm^{-2} at an overpotential of 490 mV. Interestingly, V_O-$Mo_xCo_{3-x}O_4$ displays an overpotential of 420 mV to attain 10 mA cm^{-2}. Additionally, it only requires an overpotential of 490 mV to achieve a current density of 100 mA cm^{-2}. It suggests that the activity of Co_3O_4 can be significantly enhanced by constructing oxygen vacancies *via* doping Mo into the lattice. As shown in Fig. 3b, V_O-Mo_x-$Co_{3-x}O_4$ exhibits the lowest Tafel slope of only 102.5 mV dec^{-1} compared to those of Co_3O_4 (121.8 mV dec^{-1}), and Ir/C (164.7 mV dec^{-1}), indicating fastest kinetics of OER process.[43] As shown in Fig. 3c, Vo-$Mo_xCo_{3-x}O_4$ is at a similar level in terms of activity (overpotential to achieve 10 mA cm^{-2}) and kinetics (Tafel slope) when compared with recently reported state-of-the-art non-precious metal electrocatalysts for acidic OER (Table S3, ESI†). Furthermore, compared to Co_3O_4 and Ir/C, as-synthesized V_O-$Mo_xCo_{3-x}O_4$ possesses larger electrochemical surface area (ECSA)-normalized current density, turnover frequency (TOF), and mass-activity, and a smaller reaction resistance for acidic OER (Fig. S11–S13 and Table S4, ESI†). This implies that V_O-$Mo_xCo_{3-x}O_4$ exhibits a higher intrinsic activity towards acidic OER.[44] To assess the stability of the OER in acids, the chronopotentiometric curves of V_O-$Mo_xCo_{3-x}O_4$ and Co_3O_4 were obtained at 10 mA cm^{-2} (Fig. 3d). The initial potential of 1.65 V *vs.* RHE for V_O-$Mo_xCo_{3-x}O_4$ is observed to only increase to 1.72 V *vs.* RHE after 30 h. Moreover, it is noticed that the morphology, valence states, and crystal structure of V_O-Mo_x-$Co_{3-x}O_4$ were unchanged before and after the stability test, suggesting high structural stability of the catalyst (Fig. S14–17, ESI†). However, the initial potential of Co_3O_4 is 1.70 V *vs.* RHE

and the potential rapidly increases to 2.4 V *vs.* RHE after 6.1 h, completely losing its catalytic capability. Consequently, the as-prepared V_O-$Mo_xCo_{3-x}O_4$ is at a similar level compared with the current reported state-of-the-art Co-based electrocatalysts in stability for acidic OER (Table S5, ESI†). Defects in the electrocatalysts commonly harm the long-term stability of the OER in acids.[10] However, doping a small amount of Mo can supply electrons to the Co sites during the catalytic process to hinder the dissolution of Co in an acidic solution.[19]

The variations in surface reaction intermediates were examined by *in situ* electrochemical Fourier transform infrared (FT-IR) spectroscopy to investigate the mechanism of the OER (Fig. 3e, S18 and S19, ESI†). The catalysts were uniformly dispersed onto a carbon paper electrode before being assembled in an infrared reflection setup (for details see Electrochemical measurements†). As shown in Fig. 3e, when the potentials increase to approach the OER region (≥1.5 V *vs.* RHE), distinctive adsorption bands at 1126 and 1141 cm^{-1} can be detected, in the *in situ* FT-IR spectra of V_O-$Mo_xCo_{3-x}O_4$, which are observed to be potential-dependent. The intensities of these bands increase dramatically as the potential increases. This shows that the bands are formed as a function of the applied potentials. The peak at 1126 cm^{-1} is related to the generation of an O–O bond, which frequently represents the oxygen bridges between neighboring metal sites (*–O–O–*) formed in the OPM-type OER process.[11,13] Below 1.70 V *vs.* RHE, this adsorption band blue-shifts to a higher frequency as potential increases, indicating strengthened bonding of metal sites with O–O radicals,[45] while above 1.70 V *vs.* RHE, the band gradually red-shifts to a lower frequency, suggesting a weakened bonding.[46] The peak at 1141 cm^{-1} is due to linearly bound superoxide species (*–O–O), which is the intermediate before O_2 release.[13] The potential-dependent adsorption bands detected at 3691 cm^{-1} are assigned to *OH, a typical intermediate of the OPM pathway for the OER.[11] However, these characteristic peaks cannot be observed in the *in situ* FT-IR spectra of Co_3O_4, because it is extensively believed that acidic OER is catalyzed through the AEM pathway on Co_3O_4 (ref. [13]) (Fig. S18, ESI†). Doping Mo has been proven to be unable to promote the OER process on Co_3O_4 through the OPM pathway since the resulting larger Co–Co distance inhibits direct O–O radical coupling, as shown by the results of EXAFS.[13,19] Thus, creating oxygen vacancies in the lattice is considered to be the key to inducing the OPM.

To investigate the proton–electron transfer kinetics, the acidic OER activities of V_O-$Mo_xCo_{3-x}O_4$ and Co_3O_4 were determined at pH values of 0, 0.3, 0.7, and 1.0 (Fig. 3f, g, and S20, ESI†).[47–51] V_O-$Mo_xCo_{3-x}O_4$ exhibits a stronger pH-dependent feature compared to Co_3O_4. Generally, it is an important parameter to evaluate the degree of proton reaction on the RHE scale which is used to calculate the current densities on the log scale as a function of pH ($\rho^{RHE} = \partial(\log j)/\partial pH$) (Fig. 3h and S20, ESI†).[47] Fig. 3i presents the relationship between the ratios of ρ^{RHE} (ρ^{RHE} V_O-$Mo_xCo_{3-x}O_4$/ρ^{RHE} Co_3O_4) obtained on V_O-$Mo_xCo_{3-x}O_4$ and Co_3O_4 at 1.650, 1.675, 1.700, 1.725, and 1.750 V *vs.* RHE, respectively. As a result, Co_3O_4 presents a lower ρ^{RHE} at the OER ranging from 1.650 to 1.750 V *vs.* RHE as compared with those of V_O-$Mo_xCo_{3-x}O_4$, implying a lower degree of decoupled proton–electron transfer during the rate determining step (RDS) of the AEM, *i.e.*, the deprotonation of *OOH. In contrast, higher values of ρ^{RHE} suggest a unrelated proton–electron transfer process on V_O-$Mo_xCo_{3-x}O_4$, which means a strong involvement of the OPM pathway during the OER. Furthermore, the ρ^{RHE} V_O-$Mo_xCo_{3-x}O_4$/ρ^{RHE} Co_3O_4 begins to increase gradually as the potential increases and reaches its maximum value of 2.15 at 1.700 V *vs.* RHE before descending. This indicates that at 1.70 V *vs.* RHE, participation of the OPM pathway in acidic OER on V_O-$Mo_xCo_{3-x}O_4$ is at its maximum.

The mechanism of the OER was clarified by electrochemical *in situ* Raman spectroscopy as well (Fig. 3j and S21, ESI†). The A_{1g} modes on the *in situ* Raman spectra of V_O-$Mo_xCo_{3-x}O_4$ have been found to redshift compared with those of Co_3O_4 at each applied potential. This means that oxygen vacancies are still present in the as-prepared V_O-$Mo_xCo_{3-x}O_4$ during the OER process.[24] When compared to the open-circuit potential (OCP), the *in situ* Raman spectra of Co_3O_4 at potentials from 1.3 to 1.9 V *vs.* RHE remain unchanged, exhibiting characteristic bands of spinel oxides.[16] However, the A_{1g} band in the *in situ* Raman spectrum of V_O-$Mo_xCo_{3-x}O_4$, the characteristic peak of octahedral sites, is found to gradually redshift from 692 cm^{-1} at 1.3 V *vs.* RHE to 687 cm^{-1} at 1.6 V *vs.* RHE. This usually represents the formation of highly active species of Co^{4+} in octahedral interstices during the OER process.[52] Generally, the tetravalent species are in favour of the fast deprotonation of hydroxyl by facilitating the hybridization of their t_{2g} orbitals with the O 2p band. This ultimately boosts the direct O–O radical coupling.[53,54] This is the reason why the most strengthened bonding of *–O–O–* can be detected and the strongest participation of the OPM pathway has been found at approximately 1.7 V *vs.* RHE.

To clarify the origin of enhanced activity on V_O-$Mo_xCo_{3-x}O_4$, density functional theory (DFT) simulations were performed to investigate the reaction thermodynamics and equilibrium variation during the OER process (Fig. 4). Two types of computational models were established, including Mo-doped oxygen vacancy enriched Co_3O_4 and pure Co_3O_4, representing V_O-$Mo_xCo_{3-x}O_4$ and Co_3O_4, respectively (Fig. S22 and S23, ESI†). Commonly, the OER process on the surface of electrocatalysts *via* the AEM pathway involves the adsorption and transformation of three key reaction intermediates of *OH, *O, and *OOH, as depicted in Fig. 4a.[7] As shown in Fig. 4b, the Gibbs free energy diagrams of the OER through the AEM pathway on V_O-$Mo_xCo_{3-x}O_4$ and Co_3O_4 are constructed based on the optimized structures and the energies of the adsorbed intermediates on the surfaces (Fig. S22 and S23, ESI†). It can be concluded that V_O-$Mo_xCo_{3-x}O_4$ possesses a lower free energy increase of 2.22 eV than Co_3O_4 (3.05 eV), indicating a better activity *via* the AEM (Fig. 4c). It should be noted that the process of transforming *O into *OOH is frequently deemed to be the potential-determining step (PDS), according to the scaling relationship.[7] On the other hand, the key catalytic process during the OPM pathway is generally believed to be a synergistic proton–electron-transfer reaction, involving the adsorptions of hydroxyl species (OH*–* and OH*–*OH), sequential deprotonations

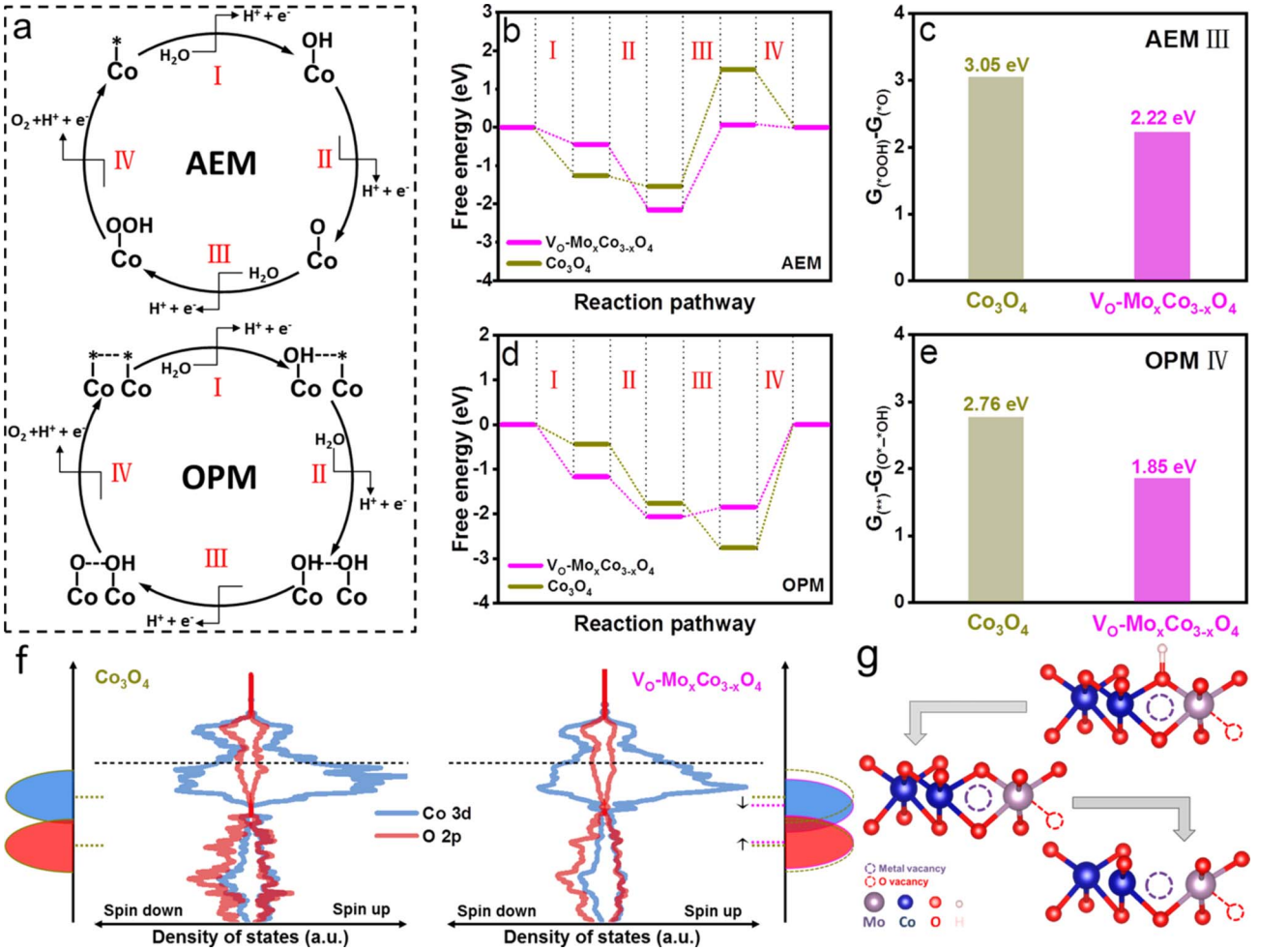

Fig. 4 (a) Schematic illustration of mechanisms for the OER through AEM and OPM pathways. (b) Gibbs free energy diagrams of the AEM pathway on V_O-$Mo_xCo_{3-x}O_4$ and Co_3O_4. (c) Histogram of free energy increases of Co_3O_4 and V_O-$Mo_xCo_{3-x}O_4$ during the PDS of the AEM pathway (AEM III) at $U = 1.23$ V. (d) Gibbs free energy diagrams of the OPM pathway on V_O-$Mo_xCo_{3-x}O_4$ and Co_3O_4. (e) Histogram of free energy increases of Co_3O_4 and V_O-$Mo_xCo_{3-x}O_4$ during the PDS of the OPM pathway (OPM IV) at $U = 1.23$ V. (f) The curves of density of states and schematic diagrams of Co 3d and O 2p orbitals in V_O-$Mo_xCo_{3-x}O_4$ and Co_3O_4. (g) The optimized structures of key intermediates adsorbed on the surface of V_O-$Mo_xCo_{3-x}O_4$ during the OPM pathway.

(O*–*OH and O*–*O), and ultimately directly coupling to O–O radicals for the generation of O_2, as presented in Fig. 4a.[11] The Gibbs free energy diagrams of the OPM pathway for the OER on V_O-$Mo_xCo_{3-x}O_4$ and Co_3O_4 are displayed in Fig. 4d, which are obtained based on the optimized structures and energies (Fig. S22 and S23, ESI†). The process of O–O radical coupling to generate O_2 is proven to be the PDS.[11] V_O-$Mo_xCo_{3-x}O_4$ shows a minimal free energy increase of 1.85 eV, which is lower than that of Co_3O_4 (2.76 eV) (Fig. 4e). Meanwhile, the superiority of the OPM over the AEM has been demonstrated, owing to the lower free energy increase.

The density of states (DOS) and band centers of Co 3d and O 2p orbitals were calculated to provide insight into the difference in the electronic structures of V_O-$Mo_xCo_{3-x}O_4$ and Co_3O_4 (Fig. 4f and S24, ESI†). Below the Fermi level, a downshifting Co 3d band and an upshifting O 2p band can be found when compared with Co_3O_4, indicating a more significant overlap of Co 3d and O 2p orbitals.[9] Generally, this will strengthen the metal–oxygen bonds in the lattice, thereby reducing the possibility of the LOM occurring on the surface of V_O-$Mo_xCo_{3-x}O_4$.[20] At the same time, the downshifting Co 3d band facilitates the hybridization of its t_{2g} orbitals with unbounded O 2p orbitals, which is beneficial for the adsorption of hydroxyl as well as deprotonation to form *O.[54] Due to the appropriate distance between the closest Co_{oct} in V_O-$Mo_xCo_{3-x}O_4$, neighboring adsorbed oxygen species will tend to directly couple for the formation of O–O radicals,[13] as exhibited in Fig. 4g. Thus, constructing oxygen vacancies by doping Mo tends to push the thermodynamic equilibrium of the OER positively and decreases the free energy increase of the PDS, ultimately lowering the overpotential of the OER process.

Conclusions

In summary, an approach of doping a small amount of Mo heteroatoms (~0.5 wt%) into Co_3O_4 was reported to enhance

the activity of the OER in acids. It has been experimentally proved that the doping can activate lattice oxygen which can be etched away from the lattice afterward for building oxygen vacancies. The achieved oxygen vacancies boost the faster OPM pathway, and simultaneously Mo with variable valence states can promote the stability. EPR results demonstrated the successful creation of oxygen vacancies in doped Co_3O_4. Synchrotron radiation characterization confirmed the variations of the valence states and coordination environments as well as bond lengths. As a result, as-synthesized Mo-doped oxygen vacancy enriched Co_3O_4 (V_O-$Mo_xCo_{3-x}O_4$) exhibited the most efficient catalytic activity (requires overpotentials of 420 and 490 mV to reach 10 and 100 mA cm^{-2}, respectively) and fastest kinetics (a Tafel slope of only 102.5 mV dec^{-1}) for the OER in an acidic medium, as compared with those of Co_3O_4 and Ir/C. V_O-$Mo_xCo_{3-x}O_4$ towards acidic OER exhibited high stability and can maintain a current density of 10 mA cm^{-2} for 30 h. Detailed electrochemical *in situ* investigations revealed that the OPM pathway for the OER was enhanced by building oxygen vacancies, due to directly observing the key reaction intermediates of *–O–O–*, *–O–O, and *OH. Meanwhile, owing to the generation of tetravalent species, which was beneficial for the adsorption as well as deprotonation of hydroxyl, the strongest participation of the OPM pathway has been found at approximately 1.7 V *vs.* RHE. Further DFT calculations clarified that the tuned Co 3d and O 2p orbitals suppressed the LOM pathway and enhanced the adsorption and rapid deprotonation of hydroxyl (the key intermediate), facilitating direct O–O radical coupling and ultimately, the promotion of the OPM pathway. This study is of significance for designing and developing highly efficient and stable non-precious metal electrocatalysts for the OER in an acidic medium, thus promoting the large-scale applications of PEMWEs.

Author contributions

X. Y. and S. H. proposed the concept and supervised the work. L. S. synthesized the materials and performed the experiments with the help of M. F., Y. P., X. Z. and Y. S.; X. Y. and S. H. analyzed the data and co-wrote the manuscript. All authors discussed the results and commented on the manuscript.

Conflicts of interest

There are no conflicts to declare.

Acknowledgements

This work was financially supported by the National Natural Science Foundation of China (51920105004), the Natural Science Foundation of Guangdong Province (2023A1515030188), the Science and Technology Program of Guangzhou (2023A04J1373), and the Special Fund for the Cultivation of Guangdong College Students' Scientific and Technological Innovation ("Climbing Program" Special Funds, pdjh2023a0160).

Notes and references

1 Y. Chen, H. Li, J. Wang, Y. Du, S. Xi, Y. Sun, M. Sherburne, J. W. Ager, A. C. Fisher and Z. J. Xu, *Nat. Commun.*, 2019, **10**, 572.
2 J. Wang, L. Han, B. Huang, Q. Shao, H. L. Xin and X. Huang, *Nat. Commun.*, 2019, **10**, 5692.
3 H. N. Nong, T. Reier, H.-S. Oh, M. Gliech, P. Paciok, T. H. T. Vu, D. Teschner, M. Heggen, V. Petkov, R. Schlögl, T. Jones and P. Strasser, *Nat. Catal.*, 2018, **1**, 841–851.
4 T. Reier, H. N. Nong, D. Teschner, R. Schlögl and P. Strasser, *Adv. Energy Mater.*, 2016, **7**, 1601275.
5 J. Feng, F. Lv, W. Zhang, P. Li, K. Wang, C. Yang, B. Wang, Y. Yang, J. Zhou, F. Lin, G. C. Wang and S. Guo, *Adv. Mater.*, 2017, **29**, 1703798.
6 X. Yang, H. Li, A.-Y. Lu, S. Min, Z. Idriss, M. N. Hedhili, K.-W. Huang, H. Idriss and L.-J. Li, *Nano Energy*, 2016, **25**, 42–50.
7 J. Yu, Q. He, G. Yang, W. Zhou, Z. Shao and M. Ni, *ACS Catal.*, 2019, **9**, 9973–10011.
8 J. Song, C. Wei, Z.-F. Huang, C. Liu, L. Zeng, X. Wang and Z. J. Xu, *Chem. Soc. Rev.*, 2020, **49**, 2196–2214.
9 K. Xiao, Y. Wang, P. Wu, L. Hou and Z. Q. Liu, *Angew. Chem., Int. Ed.*, 2023, **62**, e202301408.
10 C. Roy, R. R. Rao, K. A. Stoerzinger, J. Hwang, J. Rossmeisl, I. Chorkendorff, Y. Shao-Horn and I. E. L. Stephens, *ACS Energy Lett.*, 2018, **3**, 2045–2051.
11 C. Lin, J.-L. Li, X. Li, S. Yang, W. Luo, Y. Zhang, S.-H. Kim, D.-H. Kim, S. S. Shinde, Y.-F. Li, Z.-P. Liu, Z. Jiang and J.-H. Lee, *Nat. Catal.*, 2021, **4**, 1012–1023.
12 J. Liang, X. Gao, K. Xu, J. Lu, D. Liu, Z. Zhao, E. C. M. Tse, Z. Peng, W. Zhang and J. Liu, *Small*, 2023, 2304889.
13 N. Wang, P. Ou, R. K. Miao, Y. Chang, Z. Wang, S.-F. Hung, J. Abed, A. Ozden, H.-Y. Chen, H.-L. Wu, J. E. Huang, D. Zhou, W. Ni, L. Fan, Y. Yan, T. Peng, D. Sinton, Y. Liu, H. Liang and E. H. Sargent, *J. Am. Chem. Soc.*, 2023, **145**, 7829–7836.
14 M. Okamura, M. Kondo, R. Kuga, Y. Kurashige, T. Yanai, S. Hayami, V. K. K. Praneeth, M. Yoshida, K. Yoneda, S. Kawata and S. Masaoka, *Nature*, 2016, **530**, 465–468.
15 F. Song, M. M. Busch, B. Lassalle-Kaiser, C.-S. Hsu, E. Petkucheva, M. Bensimon, H. M. Chen, C. Corminboeuf and X. Hu, *ACS Cent. Sci.*, 2019, **5**, 558–568.
16 K. Natarajan, E. Munirathinam and T. C. K. Yang, *ACS Appl. Mater. Interfaces*, 2021, **13**, 27140–27148.
17 A. Li, S. Kong, C. Guo, H. Ooka, K. Adachi, D. Hashizume, Q. Jiang, H. Han, J. Xiao and R. Nakamura, *Nat. Catal.*, 2022, **5**, 109–118.
18 S. Anantharaj, K. Karthick and S. Kundu, *Inorg. Chem.*, 2019, **58**, 8570–8576.
19 W. Han, Y. Qian, F. Zhang, Y. He, P. Li and X. Zhang, *Chem. Eng. J.*, 2023, **473**, 145353.
20 Z. He, J. Zhang, Z. Gong, H. Lei, D. Zhou, N. Zhang, W. Mai, S. Zhao and Y. Chen, *Nat. Commun.*, 2022, **13**, 2191.
21 Y. Qi, X. Xiao, Y. Mei, L. Xiong, L. Chen, X. Lin, Z. Lin, S. Sun, B. Han, D. Yang, Y. Qin and X. Qiu, *Adv. Funct. Mater.*, 2022, **32**, 2111615.

22 S. K. Tripathy, M. Christy, N.-H. Park, E.-K. Suh, S. Anand and Y.-T. Yu, *Mater. Lett.*, 2008, **62**, 1006–1009.
23 J. Shan, C. Ye, S. Chen, T. Sun, Y. Jiao, L. Liu, C. Zhu, L. Song, Y. Han, M. Jaroniec, Y. Zhu, Y. Zheng and S.-Z. Qiao, *J. Am. Chem. Soc.*, 2021, **143**, 5201–5211.
24 J. Qian, X. Liu, C. Zhong, G. Xu, H. Li, W. Zhou, B. You, F. Wang, D. Gao and D. Chao, *Adv. Funct. Mater.*, 2023, **33**, 2212021.
25 W. Zhu, F. Yao, K. Cheng, M. Zhao, C.-J. Yang, C.-L. Dong, Q. Hong, Q. Jiang, Z. Wang and H. Liang, *J. Am. Chem. Soc.*, 2023, **145**, 17995–18006.
26 Z. Xiong, B. Tang, Z. Fang, C. Yang and S. Zhang, *J. Alloys Compd.*, 2017, **723**, 580–588.
27 X. Wu, W. Wang, N. Song, X. Yang, S. Khaimanov and N. Tsidaeva, *Chem. Eng. J.*, 2016, **306**, 382–392.
28 M.-M. Wang, L.-J. Liu, J.-R. Xi, Y. Ding, P.-X. Liu, L. Mao, B.-J. Ni, W.-K. Wang and J. Xu, *Chem. Eng. J.*, 2023, **451**, 138605.
29 Z. Hou, C. Cui, Y. Li, Y. Gao, D. Zhu, Y. Gu, G. Pan, Y. Zhu and T. Zhang, *Adv. Mater.*, 2023, **35**, 2209876.
30 L. Chong, J. Wen, E. Song, Z. Yang, I. D. Bloom and W. Ding, *Adv. Energy Mater.*, 2023, **13**, 2302306.
31 Z. Li, Y. Zhang, Y. Feng, C. Q. Cheng, K. W. Qiu, C. K. Dong, H. Liu and X. W. Du, *Adv. Funct. Mater.*, 2019, **29**, 1903444.
32 C. Hao, X. Li, H. Huang, L. Ge, Z. Fu, Y. Lu, Y. Wang, S. Zhang and Z. Cheng, *ACS Energy Lett.*, 2023, **8**, 4506–4513.
33 L. Li, X. Cao, J. Huo, J. Qu, W. Chen, C. Liu, Y. Zhao, H. Liu and G. Wang, *J. Energy Chem.*, 2023, **76**, 195–213.
34 J. Wang, J. Liu, B. Zhang, F. Cheng, Y. Ruan, X. Ji, K. Xu, C. Chen, L. Miao and J. Jiang, *Nano Energy*, 2018, **53**, 144–151.
35 Y. Zhang, Z. Zhang, G. Jiang, A. H. Mamaghani, S. Sy, R. Gao, Y. Jiang, Y. Deng, Z. Bai, L. Yang, A. Yu and Z. Chen, *Nano Energy*, 2022, **100**, 107425.
36 X. Li, L. Ge, Y. Du, H. Huang, Y. Ha, Z. Fu, Y. Lu, W. Yang, X. Wang and Z. Cheng, *ACS Nano*, 2023, **17**, 6811–6821.
37 J. Zhang, J. Qian, J. Ran, P. Xi, L. Yang and D. Gao, *ACS Catal.*, 2020, **10**, 12376–12384.
38 Z.-F. Huang, J. Song, Y. Du, S. Xi, S. Dou, J. M. V. Nsanzimana, C. Wang, Z. J. Xu and X. Wang, *Nat. Energy*, 2019, **4**, 329–338.
39 T. Wu, S. Sun, J. Song, S. Xi, Y. Du, B. Chen, W. A. Sasangka, H. Liao, C. L. Gan, G. G. Scherer, L. Zeng, H. Wang, H. Li, A. Grimaud and Z. J. Xu, *Nat. Catal.*, 2019, **2**, 763–772.
40 L. An, H. Zhang, J. Zhu, S. Xi, B. Huang, M. Sun, Y. Peng, P. Xi and C. H. Yan, *Angew. Chem., Int. Ed.*, 2023, **62**, e202214600.
41 M. Feng, J. Huang, Y. Peng, C. Huang, X. Yue and S. Huang, *ACS Nano*, 2022, **16**, 13834–13844.
42 C. Spöri, P. Briois, H. N. Nong, T. Reier, A. Billard, S. Kühl, D. Teschner and P. Strasser, *ACS Catal.*, 2019, **9**, 6653–6663.
43 Y. Peng, C. Huang, J. Huang, M. Feng, X. Qiu, X. Yue and S. Huang, *Adv. Funct. Mater.*, 2022, **32**, 2201011.
44 X. Yue, X. Qin, Y. Chen, Y. Peng, C. Liang, M. Feng, X. Qiu, M. Shao and S. Huang, *Adv. Sci.*, 2021, **8**, 2101653.
45 B. Qiao, A. Wang, X. Yang, L. F. Allard, Z. Jiang, Y. Cui, J. Liu, J. Li and T. Zhang, *Nat. Chem.*, 2011, **3**, 634–641.
46 M. Zhang, M. de Respinis and H. Frei, *Nat. Chem.*, 2014, **6**, 362–367.
47 L. Giordano, B. Han, M. Risch, W. T. Hong, R. R. Rao, K. A. Stoerzinger and Y. Shao-Horn, *Catal. Today*, 2016, **262**, 2–10.
48 A. K. Tomar, U. N. Pan, N. H. Kim and J. H. Lee, *ACS Energy Lett.*, 2023, **8**, 565–573.
49 R. Chen, Z. Wang, S. Chen, W. Wu, Y. Zhu, J. Zhong and N. Cheng, *ACS Energy Lett.*, 2023, **8**, 3504–3511.
50 Z.-M. Wang, Q.-L. Hong, X.-H. Wang, H. Huang, Y. Chen and S.-N. Li, *Acta Phys.-Chim. Sin.*, 2023, **39**, 2303028.
51 Q. Xue, Z. Wang, Y. Ding, F. Li and Y. Chen, *Chin. J. Catal.*, 2023, **45**, 6.
52 J. Huang, H. Sheng, R. D. Ross, J. Han, X. Wang, B. Song and S. Jin, *Nat. Commun.*, 2021, **12**, 3036.
53 X. L. Liu, Y. C. Jiang, J. T. Huang, W. Zhong, B. He, P. J. Jin and Y. Chen, *Carbon Energy*, 2023, **5**, e367.
54 N. Zhang, X. Feng, D. Rao, X. Deng, L. Cai, B. Qiu, R. Long, Y. Xiong, Y. Lu and Y. Chai, *Nat. Commun.*, 2020, **11**, 4066.

